



Spatiotemporal Dynamics of Urban Heat Vulnerability in Kushtia, Bangladesh (2010–2024) Using Environmental Indices and Population Data

Md. Rahedul Islam^{ID}, Mahmuda Hossain Mou^{ID}, Tamanna Yesmin^{ID}, Rabeya Sultana^{ID},
Md. Anik Hossain^{ID}*

Department of Environmental Science and Geography, Islamic University, 7003 Kushtia, Bangladesh

* Correspondence: Md. Anik Hossain (mahossain@std.iu.ac.bd)

Received: 11-26-2025

Revised: 04-01-2026

Accepted: 04-16-2026

Citation: Islam, M. R., Mou, M. H., Yesmin, T., Sultana, R., & Hossain, M. A. (2026). Spatiotemporal dynamics of urban heat vulnerability in Kushtia, Bangladesh (2010–2024) using environmental indices and population data. *Chall. Sustain.*, 14(2), 406–423. <https://doi.org/10.56578/cis140212>.



© 2026 by the author(s). Published by Acadlore Publishing Services Limited, Hong Kong. This article is available for free download and can be reused and cited, provided that the original published version is credited, under the CC BY 4.0 license.

Abstract: Rapid urbanization and land-use transformation have intensified thermal stress in mid-sized cities of Bangladesh; however, spatially explicit environmental screening of heat-related risk remains limited. This study investigates the spatiotemporal dynamics of urban heat risk in Kushtia District from 2010 to 2024 using an environmentally weighted, indicator-based geospatial framework integrating remote sensing and demographic data. Multi-temporal Landsat (Thematic Mapper (TM); Operational Land Imager (OLI); OLI/Thermal Infrared (TIRS)) and WorldPop datasets were employed to derive five environmental indices: Land Surface Temperature (LST), Albedo, Urban Thermal Field Variance Index (UTFVI), Normalized Difference Vegetation Index (NDVI), and Normalized Difference Water Index (NDWI), along with Population Density as a proxy indicator of human concentration. A composite Heat Vulnerability Index (HVI) was developed using Principal Component Analysis (PCA) to integrate these environmental and demographic variables into a spatial heat-risk surface. Results indicate a substantial rise in LST (>5 °C), particularly across urban centers such as Kushtia Sadar and Khoksa, alongside a consistent decline in NDVI and NDWI, signifying degradation of green and blue spaces. Correlation analysis revealed strong negative relationships between NDVI–LST and NDWI–LST, underscoring the mitigating role of vegetation and surface moisture. PCA results confirmed that vegetation–moisture interactions dominate environmental variability, while demographic concentration exerts a secondary yet persistent influence. High and very high heat-risk zones expanded from 211.89 km² in 2010 to 424.42 km² in 2024, reflecting intensifying spatial thermal stress. The findings represent an environmentally weighted spatial screening of heat risk rather than a comprehensive socio-ecological vulnerability assessment. The study highlights priority areas for nature-based adaptation strategies, including urban greening, waterbody restoration, and reflective surface planning, to reduce localized heat exposure in rapidly urbanizing regions of Bangladesh.

Keywords: Heat vulnerability; Principal component analysis; Geospatial analysis; Remote sensing; Climate adaptation

1. Introduction

Global climate change is accelerating the frequency, duration, and intensity of heatwaves across South Asia (Alam, 2024; Rashid et al., 2024). Bangladesh is already experiencing this shift: April 2024 marked the hottest month on record, with severe heatwaves affecting nearly 80% of the country (Alam, 2024). Since 1980, the nation's maximum temperature has increased by approximately 1.1 °C, amplifying risks to human health, livelihoods, and infrastructure (World Bank Group, 2025). Densely populated urban areas with inadequate infrastructure face particularly elevated heat risk (Zhang et al., 2025). In Bangladesh, urban communities characterized by high population density, poor housing quality, and limited access to services are consistently identified as highly susceptible to extreme heat and other climate stressors.

Within Bangladesh, the southwestern region, including Kushtia District, stands out as a climate-sensitive hotspot. Kushtia experiences substantial thermal variation, with temperatures ranging from about 11.2 °C to

37.8 °C, and it faces overlapping hazards including floods, river erosion, and drought (Hossain et al., 2025a). Climate projections indicate that both peak monsoon temperatures and annual minimum temperatures will continue to rise in the region, magnifying heat-related risks in the coming decades (Hossain et al., 2025b). Heat risk assessments classify the southwest as among the most heat-sensitive areas in the country (Mehrin et al., 2025). Despite this designation, empirical research mapping and quantifying urban heat risk in Kushtia remains limited. In particular, no study has systematically examined how spatial heat risk has changed over time alongside rapid urbanization, leaving a substantial evidence gap for local adaptation planning.

Composite Heat Vulnerability Indices (HVI) are widely used to quantify and map heat risk in urban environments. Many studies integrate environmental and socio-demographic indicators using multivariate statistical methods to derive composite risk surfaces. In India, for instance, Rathi et al. (2021) constructed an HVI from 21 socio-demographic and environmental variables, finding that most households exhibited moderate to high heat risk. In Bangladesh, PCA-based assessments have been applied in Dhaka, where Uddin et al. (2019) integrated census indicators with environmental data to generate an urban heat risk index. Similarly, Shahrujjaman et al. (2025) combined MODIS-derived land surface temperature, SAR-based vegetation and soil moisture indices, and socio-economic variables to model spatial heat risk in the capital. Internationally, PCA–GIS frameworks have been recognized as robust tools for synthesizing diverse indicators into interpretable dimensions of spatial heat risk. For example, a GIS-based analysis in Osaka applied PCA to census and land use variables to identify neighborhood-level heat risk (D’Ambrosio et al., 2023). These studies underscore that heat risk is context-specific and best captured using integrative, data-driven approaches.

Building on these methodological foundations, this study applies an environmentally weighted PCA–GIS framework to assess spatial heat risk in Kushtia District. Satellite-derived thermal and environmental metrics, including land surface temperature, albedo, vegetation, and moisture indices, form the core analytical inputs, complemented by population density as a proxy indicator of human concentration. PCA is used to reduce multicollinearity and extract dominant components, which are then spatially integrated in a GIS environment to generate a composite heat risk surface. By analyzing three time periods (2010, 2017, and 2024), the study reveals how spatial heat risk has shifted during a period of rapid urban expansion. By identifying high-risk hotspots and tracing their evolution through time, this study aims to guide local planners, health authorities, and policymakers in designing targeted and effective heat adaptation strategies. Ultimately, understanding the spatiotemporal dynamics of urban heat risk is essential for protecting public health and supporting sustainable development in Bangladesh’s rapidly warming climate.

2. Methodology

2.1 Study Area

Kushtia District is located in southern Bangladesh, within the Khulna Division. The region spans from 23°42' to 24°12' N latitude and from 89°19' to 90°40' E longitude. It comprises six upazilas: Bheramara, Khoksa, Mirpur, Kumarkhali, Kushtia Sadar, and Daulatpur (Hossain et al., 2025a). The district covers a total area of 1,621.15 km² (Banglapedia, 2023). The population stands at 2,149,692, with a population density of 1,336 persons per km² and an average annual growth rate of 0.88% (Bangladesh Bureau of Statistics, 2023). The region experiences a tropical monsoon-influenced climate, marked by significant seasonal variation in precipitation. Average summer temperatures reach up to 37.8 °C, while winter lows average around 11.2 °C. The annual rainfall is approximately 1,467 mm, with most precipitation occurring during the monsoon season (Hossain et al., 2025b).

2.2 Dataset

This study utilized two types of secondary datasets: satellite imagery and population density data. The satellite images were acquired from the Landsat 5 Thematic Mapper (TM) and Landsat 8, and 9 Operational Land Imager (OLI) sensors, corresponding to path/row 138/43 and 138/44, and were sourced from the United States Geological Survey Earth Explorer portal (<https://earthexplorer.usgs.gov/>). Images were selected based on cloud cover of less than 5% to ensure data quality. Prior to analysis, all images underwent radiometric calibration and atmospheric correction to enhance their accuracy.

Three reference years, 2010, 2017, and 2024, were chosen to represent decadal, mid-term, and recent trends in land use and population distribution. Population data for 2010 and 2017 were obtained from the WorldPop open-access platform (<https://www.worldpop.org/>). Since WorldPop provides data only up to 2020, the population for 2024 was projected using an exponential growth model with an annual growth rate of 0.88%, as expressed in Eq. (1).

$$P_{2024} = P_{2020} \times 1.0088^4 \quad (1)$$

where, P_{2024} represents the estimated population for the year 2024, P_{2020} is the actual population in 2020, 1.0088

denotes the annual growth multiplier based on a growth rate of 0.88%, and 4 refers to the number of years between 2020 and 2024.

To ensure spatial consistency for raster registration and overlay analysis with 30 m satellite imagery, population data were resampled from their original 1 km spatial resolution to 30×30 m using ArcGIS 10.8, following Stevens et al. (2015). This resampling was performed solely to align the grid structure and does not increase the inherent spatial precision or represent actual 30 m population detail. Detailed information on image acquisition and associated cloud cover percentages is provided in Table 1.

The land use/land cover map (Figure 1) was derived from Landsat 8 OLI imagery for 2024, obtained from the United States Geological Survey Earth Explorer platform. A supervised classification approach using the maximum likelihood algorithm was applied to identify major land cover classes, including water bodies, settlements, vegetation, char land, and fallow land. The classification supports the analysis of spatial heat vulnerability patterns.

Table 1. Specifications of the selected Landsat images

Year	Name of Satellite	Path /Row	Acquisition Date	Cloud Cover	Resolution
2010	Landsat -5 (TM)	138/43	2010-02-06	0.00	30 m
	Landsat -5 (TM)	138/44	2010-02-06	0.00	30 m
2017	Landsat -8 (OLI & TIRS)	138/43	2017-02-09	0.02	30 m
2024	Landsat -9 (OLI & TIRS)	138/43	2024-02-29	0.02	30 m

Note: Thematic Mapper (TM); Operational Land Imager (OLI); Thermal Infrared (TIRS)

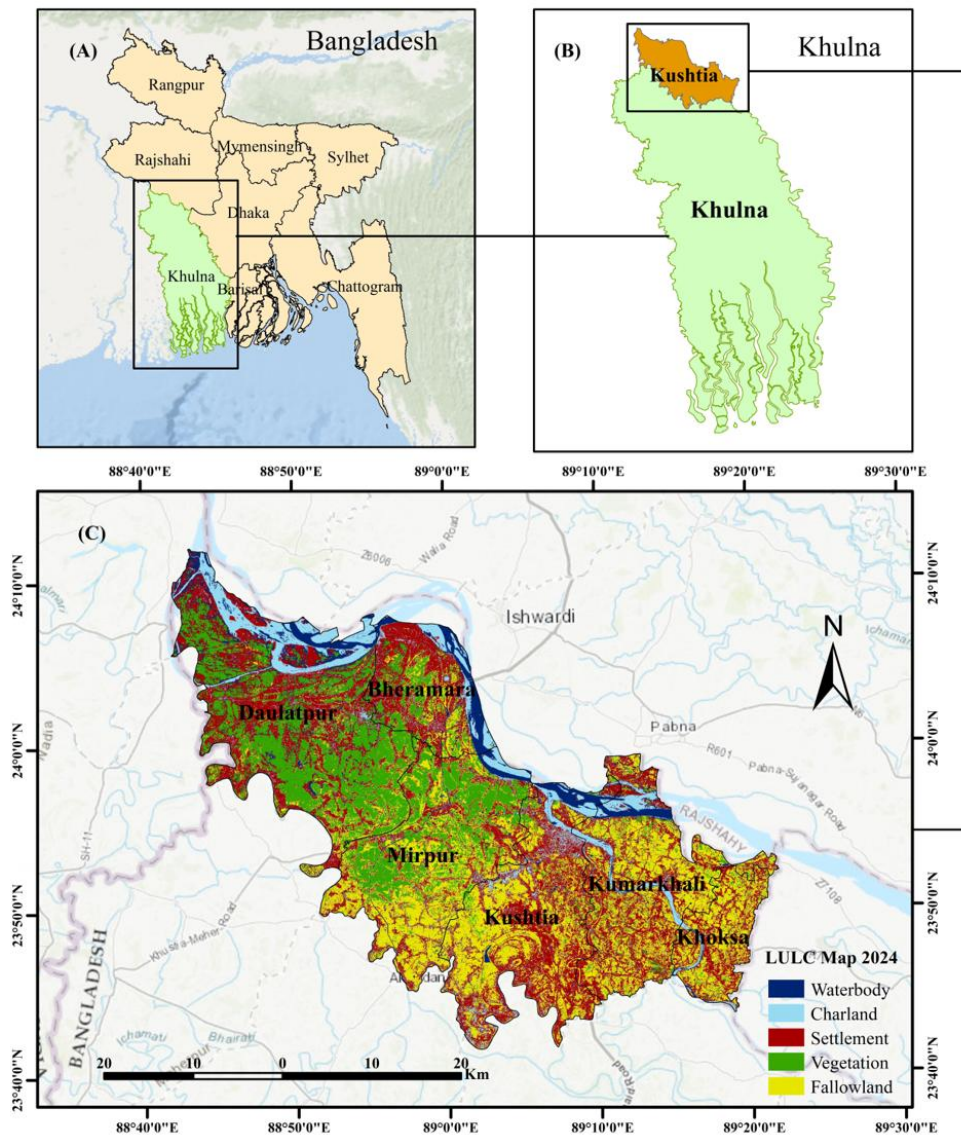


Figure 1. Geographic location of the study area and land use/land cover map

2.3 Radiometric Correction of Landsat Image

Landsat satellite data, provided as Level-1 products by the United States Geological Survey, are delivered as quantized and calibrated Digital Numbers (DNs) representing multispectral observations. To enable the physical interpretation of surface characteristics, these DNs are converted into Top-of-Atmosphere (TOA) spectral radiance and TOA reflectance. The conversion procedures vary slightly depending on the sensor type (e.g., Landsat 5 TM vs. Landsat 8 OLI). The detailed methodology for radiometric correction of Landsat imagery is presented in Table A1. Satellite images were preprocessed using ENVI 5.3 and analyzed in ArcGIS 10.8 for clipping, band selection, and conversion to TOA reflectance.

2.4 Heat Vulnerability Index Calculation

The Heat Vulnerability Index (HVI) was developed to systematically assess urban heat risk variations across different areas using an environmentally weighted, geospatial screening approach. Rather than fully implementing the Intergovernmental Panel on Climate Change vulnerability framework, this study primarily relies on satellite-derived environmental indicators and gridded population data to capture heat exposure patterns and relative susceptibility (Begum et al., 2023; Rathi et al., 2021). Five satellite-derived and population-based indicators were selected and integrated within this framework. The HVI calculation followed four sequential steps, which are described in the following sections.

2.4.1 Step 1: Indicator selection

(1) Exposure

Exposure, the degree to which urban areas and populations experience heat stress, forms a key component of the HVI (Sun et al., 2022). This study assessed exposure using three satellite-derived indicators: Land Surface Temperature (LST), Land Surface Albedo (α), and the Urban Thermal Field Variance Index (UTFVI).

LST quantifies surface heat intensity and reveals spatial patterns of thermal stress (Yang et al., 2014). It is derived from the Thermal Infrared (TIRS) bands of Landsat satellites, Band 6 for Landsat 5 TM and Landsat 7 ETM+, and Bands 10–11 for Landsat 8 TIRS, using a six-step conversion process from TOA radiance to surface temperature (Saha & Gayen, 2025). The detailed retrieval procedure is summarized in Table A2.

Albedo represents surface reflectivity and influences the Earth's surface energy balance. Low-albedo materials (e.g., asphalt, concrete) absorb more heat, intensifying the Urban Heat Island (UHI) effect, while high-albedo surfaces reflect more solar radiation, reducing heat accumulation (Elgendy et al., 2025; Zhao et al., 2025). It was estimated from Landsat reflectance data following the empirical formulas by Liang (2001) and Tasumi et al. (2008), with values ranging from 0 (perfect absorber) to 1 (perfect reflector).

Landsat 5 (B1: Blue, B2: Green, B3: Red, B4: NIR, B5: SWIR-1):

$$\alpha = \frac{0.356 * B1 + 0.130 * B2 + 0.373 * B3 + 0.085 * B4 + 0.072 * B5 - 0.018}{1.016} \quad (2)$$

Landsat 8 B2: Blue, B3: Green, B4: Red, B5: NIR, B6: SWIR-1:

$$\alpha = \frac{(0.356 \times B2 + 0.130 \times B3 + 0.373 \times B4 + 0.085 \times B5 + 0.072 \times B6 - 0.018)}{1.016} \quad (3)$$

UTFVI identifies thermal variability and ecologically stressed zones by comparing pixel-level LST with the mean surface temperature of the study area (Renard et al., 2019). It is calculated using Eq. (4):

$$UTFVI = \frac{(T_s - T_{mean})}{(T_{mean})} \quad (4)$$

where, T_s and T_{mean} represent pixel and mean LST, respectively. The index was classified into six categories of ecological and thermal stress (Table 2), following Cevik Degerli & Cetin (2023).

These indicators were selected for the Kushtia district because they are well-suited for data-scarce urban environments lacking continuous meteorological records. They can be consistently derived from freely available Landsat data, providing reliable, long-term, and spatially explicit insights into urban heat exposure. Collectively, LST, Albedo, and UTFVI capture thermal intensity, radiative behavior, and spatial variability, offering a comprehensive and cost-effective representation of heat exposure in Kushtia's rapidly urbanizing context.

(2) Sensitivity

Sensitivity reflects the extent to which a population or system is affected by heat stress, highlighting how demographic and social factors influence vulnerability (Rathi et al., 2021). In this study, population density was chosen as the primary indicator of sensitivity because it directly affects heat vulnerability. Densely populated areas

experience higher exposure due to limited open spaces, increased energy demand, and intensified anthropogenic activity, which together reduce the capacity to adapt to rising temperatures (Patwary et al., 2025). Thus, population density, in combination with exposure indices, provides a more nuanced understanding of areas at greater risk within the study area.

Table 2. Urban Thermal Field Variance Index (UTFVI) classification for ecological status and thermal stress levels

UTFVI Range	Ecological Status	Thermal Stress Level
<0.000	Excellent	No stress
0.000–0.005	Good	Low
0.005–0.010	Moderate	Moderate
0.010–0.015	Poor	High
0.015–0.020	Bad	Very high
>0.020	Worst	Extreme

Source: Kliengchuay et al. (2025)

(3) Adaptive Capacity

Adaptive capacity refers to the ability of a system or environment to cope with heat stress and mitigate its impacts (Rathi et al., 2021). In this study, NDVI (Normalized Difference Vegetation Index) and NDWI (Normalized Difference Water Index) were used to assess the environmental components of adaptive capacity. NDVI measures vegetation density, with low values indicating sparse vegetation. Areas with limited greenery are more sensitive to heat due to minimal shading and reduced cooling from plant transpiration (Huang et al., 2025). NDWI reflects surface water presence, with low values indicating limited water resources, which reduces natural cooling through evaporation (Mahim et al., 2025). Regions with both low NDVI and NDWI are therefore more vulnerable, as the environment’s natural buffering against heat is diminished. Conversely, areas with higher NDVI, NDWI, and Albedo values exhibit greater adaptive capacity, as vegetation and water bodies reduce surface heat, enhance evaporation, and mitigate urban heat accumulation.

NDVI is calculated using the difference between near-infrared (NIR) and red (RED) reflectance divided by their sum, allowing monitoring of vegetation health and density over time (Anand et al., 2025; Gessesse & Melesse, 2019). NDWI uses NIR and green (GREEN) spectral bands to detect water bodies and assess moisture-related cooling potential (Hossain et al., 2025a). The formulas and value ranges for NDVI and NDWI are summarized in Table 3.

Table 3. Equations and value ranges for Normalized Difference Vegetation Index (NDVI) and Normalized Difference Water Index (NDWI) used to assess adaptive capacity

Index	Equation	Range
NDVI	$NDVI = \frac{(NIR-Red)}{(NIR+Red)}$	[-1,+1]
NDWI	$NDWI = \frac{(Green-NIR)}{(Green+NIR)}$	[-1,+1]

Source: Hossain et al. (2025a)

This approach integrates vegetation and water indicators to quantify the environmental resilience of Kushtia Municipality, linking natural buffering capacity directly to adaptive potential against heat stress.

2.4.2 Step 2: Data preparation and normalization

All spatial indicators were first converted into raster format and resampled to ensure a uniform spatial resolution. Subsequently, the data were normalized using the min–max normalization technique to scale all variables between 0 and 1, thereby enabling meaningful comparison across different measurement units and ranges (Adnan et al., 2024). Adaptive capacity indicators such as NDVI, NDWI, and Albedo were inversely normalized to align lower vulnerability values with the overall vulnerability index. The normalization followed Eq. (5):

$$X' = \frac{X - \text{Min}(X)}{\text{Max}(X) - \text{Min}(X)} \quad (5)$$

where, X' represents the normalized value and X is the original value of the indicator.

2.4.3 Step 3: Principal Component Analysis and weight determination

Principal Component Analysis (PCA) was employed to derive objective weights for integrating the selected heat vulnerability indicators into a single composite index. This method minimizes redundancy among correlated variables by transforming them into uncorrelated orthogonal components while preserving the dominant variance

within the dataset. PCA was performed in Python 3 using a Jupyter Notebook environment on Google Colab (<https://colab.research.google.com/>). A 20×20 fishnet grid was applied to the study area to calculate the mean index value within each cell, ensuring computational efficiency and adequate spatial representation. Although PCA was performed separately for each study year to capture year-specific covariance structures, all input variables were standardized using a consistent min–max normalization approach prior to analysis. Therefore, the derived weights are comparable in terms of relative spatial interpretation across time, as they are based on uniformly scaled inputs and a consistent methodological framework.

Among the extracted components, the first principal component (PC1) consistently accounted for the largest portion of total variance across all study years and was therefore selected as the basis for deriving indicator weights (Hossain et al., 2025a). This approach ensures that the dominant variance structure within the dataset is retained while minimizing redundancy among correlated indicators. The absolute loadings of each indicator on PC1 were normalized to sum to unity, and the weight of each indicator (W_i) was computed using Eq. (6):

$$W_i = \frac{|L_{i,PC1}|}{\sum_{j=1}^n |L_{j,PC1}|} \quad (6)$$

where, $L_{i,PC1}$ is the loading of the i -th indicator on PC1, and n is the total number of indicators included in the analysis. Indicators showing stronger relationships with PC1 received higher weights, while weaker contributors had proportionally reduced influence. The PCA-derived weights were then used to compute the HVI.

2.4.4 Step 4: Heat Vulnerability Index computation and visualization

The normalized indicators were combined using a weighted linear aggregation approach to calculate the HVI as described in Eq. (7):

$$HVI = \sum(w_i \cdot x_i) \text{ Exposure} + \sum(w_j \cdot x_j) \text{ Sensitivity} - \sum(w_k \cdot x_k) \text{ Adaptive Capacity} \quad (7)$$

where, w represents the PCA-derived weights and x denotes the normalized indicator values. The resulting composite raster produced continuous values ranging from 0 (least vulnerable) to 1 (most vulnerable). The spatial analysis was performed in ArcGIS 10.8 using tools from the Spatial Analyst extension. The resulting HVI values represent relative vulnerability within each time period; therefore, spatial patterns and class distributions are comparable across years, while absolute values should be interpreted in a relative (within-year) context rather than as direct numerical equivalents. The normalized indicators were integrated through a weighted overlay approach to generate the final HVI map. The corresponding index weights and combinations are summarized in Table A3.

2.4.5 Step 5: Classification of vulnerability levels

For effective interpretation and spatial representation, HVI values were categorized into five classes following Raja et al. (2021) (Table 4). The classification delineates urban areas based on the combined effects of exposure, sensitivity, and adaptive capacity.

Table 4. Classification of vulnerability levels

Index Range	Category
0.00–0.11	Very Low
0.12–0.23	Low
0.24–0.31	Moderate
0.32–0.41	High
0.42–1.00	Very High

Source: Adnan et al. (2024); Raja et al. (2021)

2.5 Pearson’s Correlation Analysis

To evaluate the interrelationships among the selected heat vulnerability indicators, NDVI, NDWI, Albedo, UTFVI, LST, and Population Density, across different time periods, a Pearson’s correlation analysis was performed using the exact dataset used for PCA analysis. This method quantifies the strength and direction of linear relationships between variables, providing insights into how each factor influences or aligns with the overall HVI. The Pearson correlation coefficient (r) ranges from -1 to $+1$, where values near $+1$ indicate a strong positive linear relationship, values near -1 denote a strong negative linear relationship, and values close to 0 suggest no linear association between the variables (Hossain et al., 2023). The coefficient was computed using Eq. (8):

$$r = \frac{\sum(x - \bar{x})(y - \bar{y})}{\sqrt{\sum(x - \bar{x})^2 \sum(y - \bar{y})^2}} \quad (8)$$

The Pearson correlation coefficient is denoted as r . It calculates the linear relationship between two variables. x_i and y_i correspond to the values of the variables and each unit, respectively; \bar{x} represents the variable's mean; and \bar{y} signifies the mean value.

3. Results

3.1 Heat Exposure

The spatial distribution maps of thermal exposure reveal consistent and concerning trends across the study period (2010–2024). LST, shown in Figure 2(A), demonstrates a significant warming trend, with the highest temperatures consistently concentrated in the eastern and southern areas, particularly around Khoksa and Kushtia. The maximum LST rose sharply from 29.60 °C in 2010 to 34.68 °C in 2024. Simultaneously, Albedo in Figure 2(B) also experienced a notable increase in its maximum value (from 0.23 to 0.41), with high reflectivity patches becoming widespread across the central-eastern corridor. Finally, the UTFVI, depicted in Figure 2(C), confirms the LST findings, with high positive UTFVI values indicative of severe thermal discomfort firmly localized in the same eastern urban centers (Khoksa, Kumarkhali) across all analyzed years. Although maximum Land Surface Temperature (LST) increased significantly, UTFVI values remained nearly unchanged because UTFVI is a relative measure based on deviation from the mean LST. As both maximum and mean LST rose proportionally, their difference stayed nearly constant, causing minimal change in UTFVI. Collectively, these figures confirm a clear spatiotemporal expansion of thermal stress in the Kushtia district.

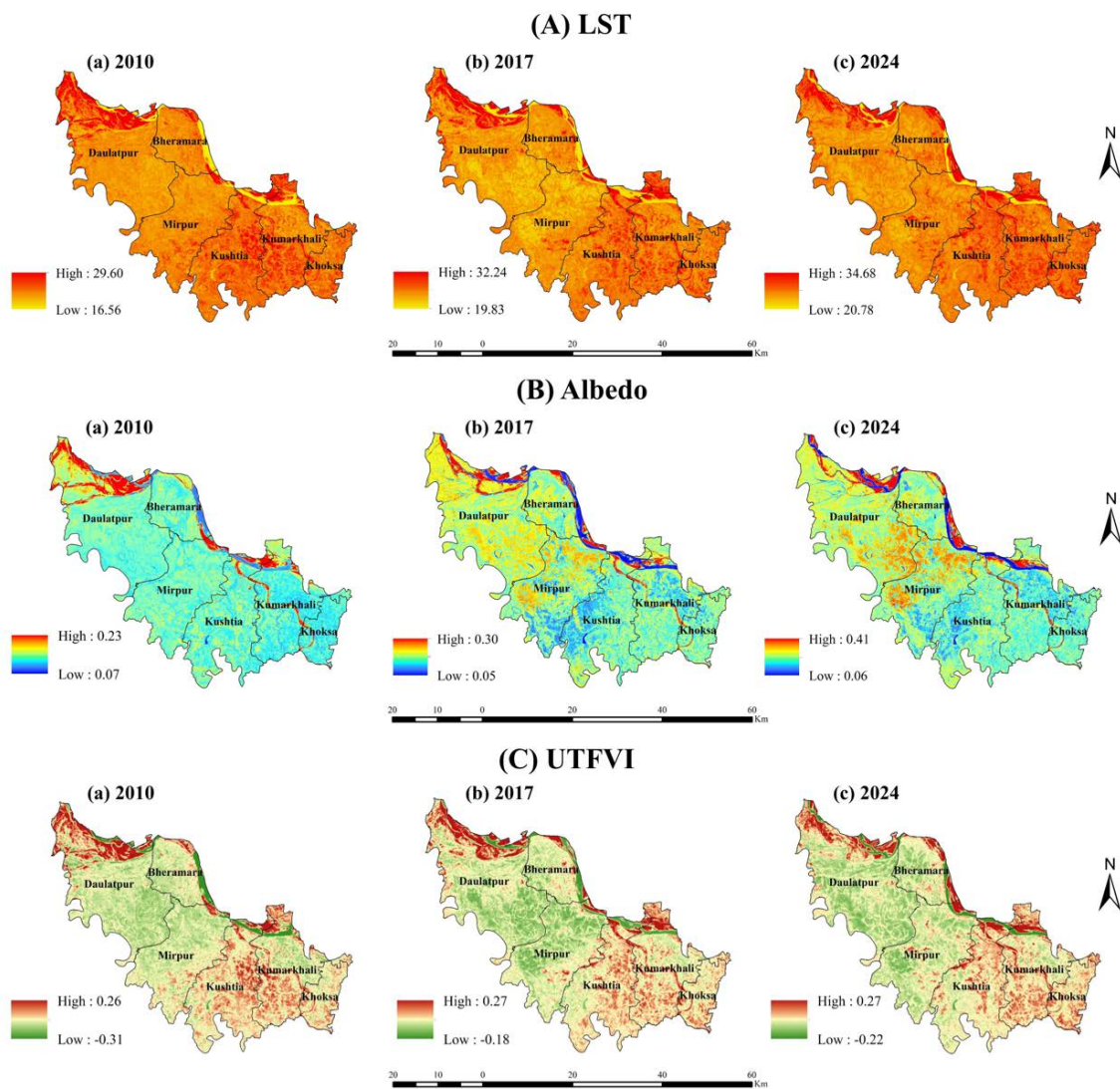


Figure 2. Spatial and temporal distribution of key thermal exposure parameters in the study area for 2010, 2017, and 2024 used in Heat Vulnerability Index (HVI) calculation. (A) Land Surface Temperature (LST), (B) Land Surface Albedo, and (C) Urban Thermal Field Variance Index (UTFVI)

District and upazila-level statistics (Table A4 and Table A5) corroborate the spatial maps, showing minor changes in surface reflectance but clear shifts in thermal exposure. LST analysis indicates a marked warming trend: low-temperature areas ($<25\text{ }^{\circ}\text{C}$) decreased from $1,562.17\text{ km}^2$ in 2010 to 793.64 km^2 in 2024, while medium-temperature areas ($25\text{--}35\text{ }^{\circ}\text{C}$) expanded from 101.91 km^2 to 870.44 km^2 ; high-temperature areas ($>35\text{ }^{\circ}\text{C}$) remained negligible. Albedo remained predominantly low (<0.3), covering $1,664.08\text{ km}^2$ in 2010 and 2017, slightly declining to $1,662.91\text{ km}^2$ in 2024, with minor medium-albedo expansion (1.17 km^2); Mirpur consistently had the lowest albedo ($\sim 328.5\text{ km}^2$) and Khoksa the lowest ($\sim 101.25\text{ km}^2$). UTFVI indicates intensifying thermal stress: low UTFVI (<0.005) shrank from $1,143.86\text{ km}^2$ to $1,039.65\text{ km}^2$, medium ($0.005\text{--}0.015$) rose to 113.40 km^2 , and high (≥ 0.015) remained substantial ($\sim 511.03\text{ km}^2$). Upazila-level shifts show high UTFVI expansion in Bheramara, Khoksa, and Kumarkhali, while Daulatpur and Kushtia declined slightly. Overall, despite stable albedo, the district experienced pronounced LST and UTFVI increases, reflecting intensifying urban thermal stress between 2010 and 2024.

3.2 Heat Sensitivity

The spatial assessment of population density highlights a growing demographic concentration and rising exposure to heat-related risks across Kushtia District. As illustrated in Figure 3, the highest densities are consistently concentrated in major municipal areas, particularly Kushtia, Kumarkhali, and Bheramara.

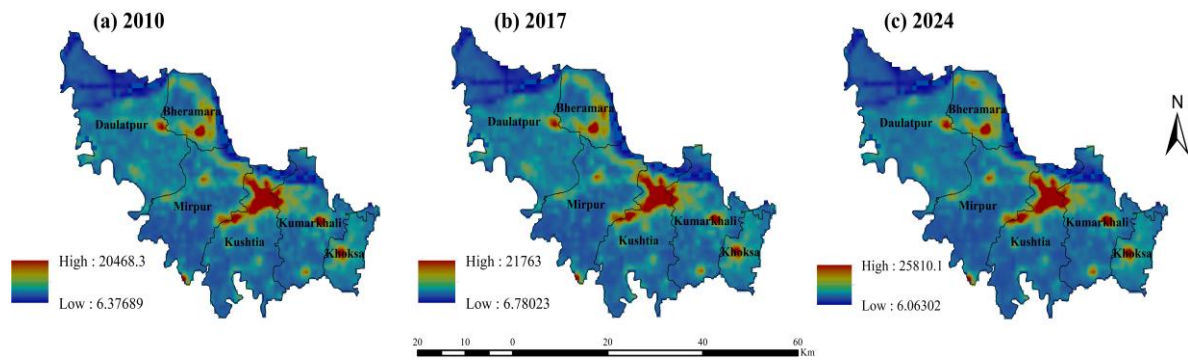


Figure 3. Spatial and temporal distribution of population density across the study area for the years (a) 2010, (b) 2017, and (c) 2024

Quantitative analysis (Table A4 and Table A5) indicates rapid urbanization, with the high-density class expanding 47.35% , from 16.81 km^2 in 2010 to 24.77 km^2 in 2024, largely driven by Kushtia Upazila, which accounted for over 68% of this area. Medium-density areas also expanded notably in surrounding upazilas such as Daulatpur and Mirpur, reflecting gradual peri-urban growth and increasing population pressure.

3.3 Heat Adaptive Capacity

The evaluation of adaptive capacity, using vegetation and surface water indices as proxies for natural cooling, reveals a declining trend throughout Kushtia District (Figure 4). Both NDVI and NDWI demonstrate significant reductions in their maximum values between 2010 and 2024, signifying a marked loss in vegetation cover and surface water extent. Specifically, the maximum NDVI decreased from 0.57 to 0.53 , while the maximum NDWI dropped sharply from 0.34 to 0.18 over the same period.

At the district scale (Table A4 and Table A5), NDVI analysis indicates a contraction of low-class (<0.2) areas from 810.22 km^2 to 560.97 km^2 , accompanied by an expansion of medium-class ($0.2\text{--}0.5$) areas from 851.67 km^2 to $1,100.42\text{ km}^2$, whereas high-class (>0.5) areas remained minimal ($2.19 \rightarrow 2.70\text{ km}^2$). Upazila-level patterns exhibit spatial heterogeneity: Mirpur retained a relatively high share of medium-class vegetation ($204.30 \rightarrow 229.56\text{ km}^2$), while Daulatpur experienced a notable increase ($316.72 \rightarrow 376.42\text{ km}^2$). High NDVI zones remained scarce, with only marginal gains in Daulatpur ($1.31 \rightarrow 0.84\text{ km}^2$) and Mirpur ($0.34 \rightarrow 1.85\text{ km}^2$). Similarly, NDWI results confirm declining surface water presence. The low-class (<0.2) area slightly expanded ($1,624.06 \rightarrow 1,664.08\text{ km}^2$), while the medium-class ($0.2\text{--}0.5$) category virtually disappeared ($40.02 \rightarrow 0\text{ km}^2$). Upazila-level NDWI remained dominated by low-class coverage in Bheramara ($139.56 \rightarrow 153.06\text{ km}^2$), Daulatpur ($480.26 \rightarrow 490.62\text{ km}^2$), and Mirpur ($326.22 \rightarrow 328.53\text{ km}^2$). Collectively, these results suggest a progressive reduction in natural cooling capacity and a diminished adaptive potential to thermal stress across Kushtia District, driven by urbanization-induced landscape alterations and the degradation of green and blue spaces.

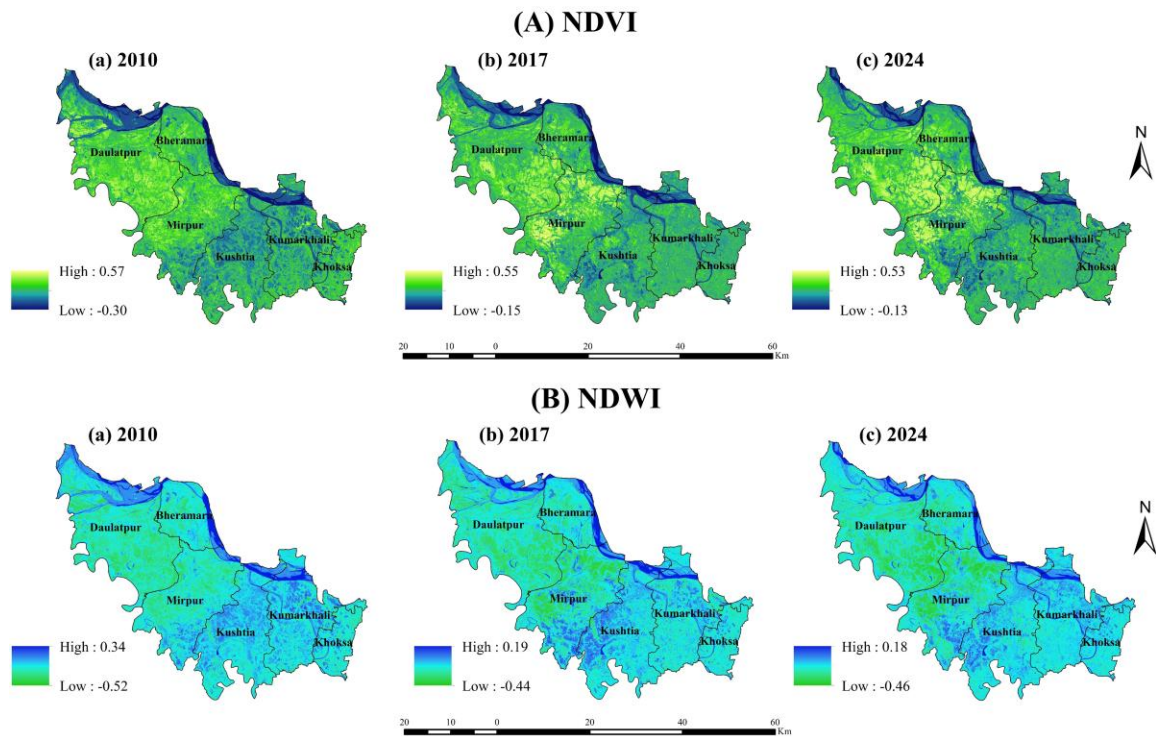


Figure 4. Spatial and temporal distribution of key adaptive capacity parameters in the study area for 2010, 2017, and 2024. (A) Normalized Difference Vegetation Index (NDVI) and (B) Normalized Difference Water Index (NDWI)

3.4 Relationship Among Indices

The correlation analysis is presented in Figure 5, illustrating the dynamic interplay between vegetation, moisture, and built-up indices with population density over 14 years. These relationships reveal spatial and temporal interactions shaping the study area.

A strong and persistent negative correlation between NDVI and LST ($r = -0.44$ in 2010, -0.34 in 2017, -0.42 in 2024, and -0.40 overall) signifies the consistent degradation of vegetation cover with increasing urbanization and demographic concentration. In contrast, LST exhibits a shifting relationship with population density. While slightly negative in 2010 ($r = -0.12$), the correlation turned positive in 2017 ($r = 0.20$) and 2024 ($r = 0.12$). Albedo maintains a stable positive association with population density ($r \approx 0.20$ in 2017–2024; $r = 0.60$ in 2010). Among the indices, the strongest inter-variable relationships were observed between NDVI and NDWI ($r = -0.99$ in 2024) and NDVI and LST ($r = -0.98$ for 2010–2024). Collectively, these results confirm that rapid urban expansion across Kushtia District has disrupted the natural equilibrium between green cover, water availability, and heat regulation.

3.5 Principal Component Analysis

The PCA results summarized in Table 5 demonstrate distinct temporal variations in the relationships among environmental and socio-economic indicators across the study period. In 2010, PC1 (54.49%) was primarily influenced by NDVI (-0.63) and NDWI (0.49). Meanwhile, PC2 (35.73%) was largely associated with LST (0.50) and UTFVI (0.52). By 2017, the pattern remained largely consistent, with PC1 (51.12%) still governed by vegetation–moisture interactions, while PC2 (38.98%) became increasingly characterized by LST, UTFVI, and Albedo. Additionally, Albedo showed a strong loading on PC3 (-0.76), and Population Density loaded on PC4 (-0.79). In 2024, this distinction became more pronounced. PC1 (63.03%) was dominated by NDVI (0.68) and NDWI (-0.62). In contrast, PC2 (30.82%) was associated with LST (0.61) and UTFVI (0.65). Furthermore, Albedo consistently loaded on PC3 (-0.88) and Population Density on PC4 (0.98). Taken together, the progressive increase in the variance explained by PC1 over time indicates a strengthening role of vegetation and surface water conditions in determining environmental variability, whereas urban and population-related factors persist as secondary yet distinct influences. Although PC2 explains a substantial proportion of variance across all periods, PC1 consistently represents the dominant gradient of variability and is therefore used as the basis for indicator weighting in the construction of the HVI.

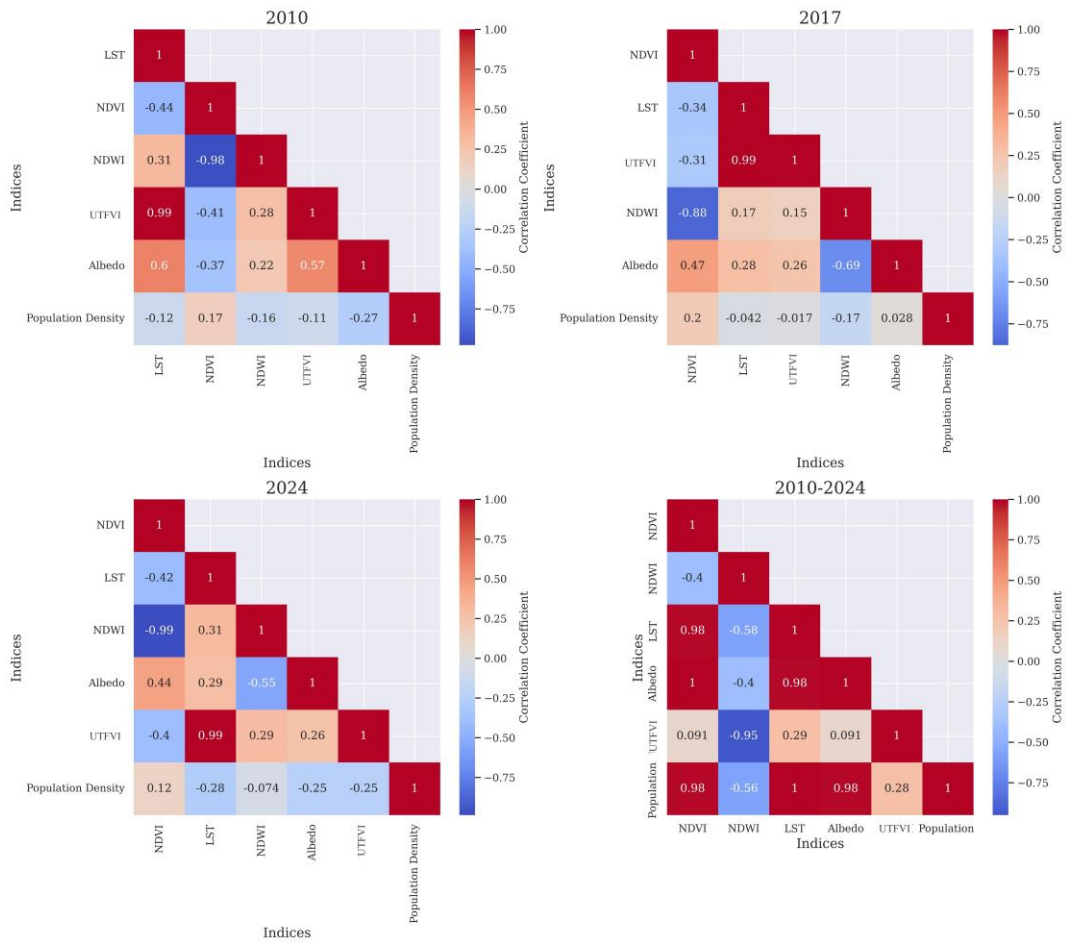


Figure 5. Correlation matrix of remote sensing indices and population density for different years (2010, 2017, and 2024) and the overall period (2010–2024)

Table 5. PCA results of heat vulnerability factors in 2010, 2017, and 2024

Year	Indicator	PC1	PC2	PC3	PC4
2010	NDVI	-0.63	0.38	0.003	-0.01
	LST	0.38	0.50	0.28	-0.04
	UTFVI	0.34	0.52	0.34	-0.0004
	NDWI	0.49	-0.46	0.08	-0.03
	Albedo	0.30	0.32	-0.88	0.10
	Population Density	-0.007	-0.02	0.10	0.99
	Eigenvalue	0.02	0.01	0.003	0.00099
2017	Percent Eigenvalue	54.49	35.73	7.09	2.31
	NDVI	-0.58	0.08	0.50	0.411
	LST	0.30	0.55	0.20	0.06
	UTFVI	0.31	0.59	0.32	-0.02
	NDWI	0.64	-0.29	-0.09	0.41
	Albedo	-0.24	0.49	-0.76	0.12
	Population Density	0.01	-0.005	0.09	-0.79
2024	Eigenvalue	0.02	0.01	0.002	0.001
	Percent Eigenvalue	51.12	38.98	5.77	2.13
	NDVI	0.68	0.11	0.27	-0.04
	LST	-0.22	0.61	0.13	-0.05
	UTFVI	-0.23	0.65	0.27	-0.05
	NDWI	-0.62	-0.21	-0.13	0.01
	Albedo	0.20	0.36	-0.88	0.15
Overall	Population Density	-0.01	0.01	0.17	0.98
	Eigenvalue	0.02	0.01	0.001	0.0008
	Percent Eigenvalue	63.03	30.82	3.98	1.98

Note: Principal Component Analysis (PCA); Normalized Difference Vegetation Index (NDVI); Land Surface Temperature (LST); Urban Thermal Field Variance Index (UTFVI); Normalized Difference Water Index (NDWI)

3.6 Heat Vulnerability

The spatial distribution of heat vulnerability in Kushtia District from 2010 to 2024 reveals notable temporal and spatial variations (Figure 6). In 2010, most areas of the district exhibited low to moderate heat vulnerability, with only small patches of high and very high vulnerability concentrated primarily in the northern and central regions, particularly around Kushtia and Daulatpur. By 2017, the extent of high and very high vulnerability zones had expanded significantly, especially in the northern and central parts of the district. However, by 2024, the pattern demonstrates slight improvement or stabilization, as some northern areas continue to experience very high vulnerability, while the southern and southwestern parts, including Khoksa and portions of Kushtia Sadar, exhibit a greater prevalence of low to moderate vulnerability zones compared to 2017. Overall, the trend suggests a substantial increase in heat vulnerability between 2010 and 2017, followed by a partial reduction or redistribution of vulnerability by 2024.

The area statistics of heat vulnerability in Kushtia District from 2010 to 2024 reveal a clear temporal shift toward higher vulnerability levels (Table 6). In 2010, the district was predominantly characterized by low (611.72 km²) and moderate (434.23 km²) vulnerability, while high and very high vulnerability areas were comparatively limited to 154.06 km² and 57.83 km², respectively. By 2017, a significant increase was observed in the high (245.53 km²) and very high (72.57 km²) categories, accompanied by a reduction in low and moderate zones. The trend continues in 2024, where high (339.44 km²) and very high (84.98 km²) vulnerability areas expand further, while the very low and low categories decline sharply to 132.52 km² and 432.17 km², respectively. However, by 2024, the pattern indicates a continued increase in vulnerability, with the expansion of high and very high vulnerability zones, particularly in northern areas, while some parts of the south and southwest, including Khoksa and portions of Kushtia Sadar, still show relatively lower to moderate vulnerability compared to other regions. Overall, the temporal progression from 2010 to 2024 reveals a clear deterioration in the district's thermal resilience, with a marked expansion of high and very high vulnerability zones in Kushtia District.

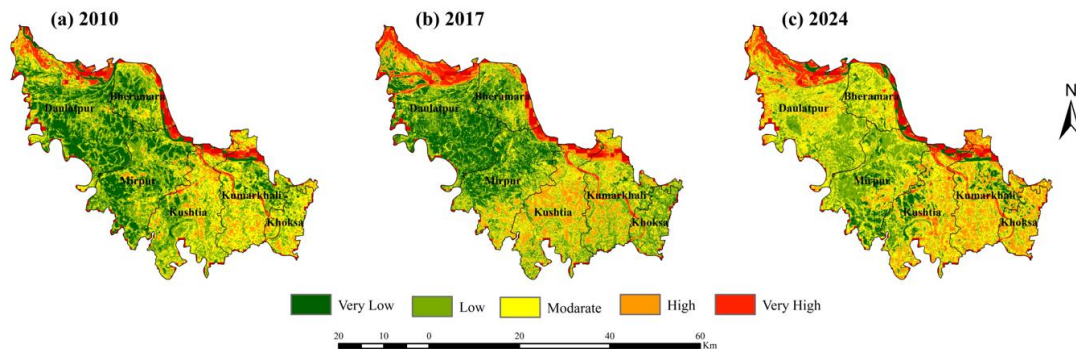


Figure 6. Spatial distribution of heat vulnerability in Kushtia District for (a) 2010, (b) 2017, and (c) 2024

Table 6. Area statistics of heat vulnerability classes in Kushtia District for the years 2010, 2017, and 2024

Year	Class	Area (Sq. km)
2010	Very Low	335.71
	Low	611.72
	Moderate	434.23
	High	154.06
	Very High	57.83
2017	Very Low	329.26
	Low	537.85
	Moderate	408.34
	High	245.53
2024	Very High	72.57
	Very Low	132.52
	Low	432.17
	Moderate	604.43
	High	339.44
	Very High	84.98

4. Discussion

In this study, the results reveal a pronounced intensification of urban heat exposure in Kushtia District between 2010 and 2024, driven by rising surface temperature, vegetation loss, and water depletion, along with the growing

dominance of heat-retaining and reflective urban surfaces. LST increased sharply—with maximum values rising from 29.6 °C to 34.7 °C—and high-heat zones became concentrated in the densely built-up eastern and southern upazilas (e.g., Khoksa, Kumarkhali). This spatial pattern is consistent with well-known UHI dynamics: rapid replacement of vegetation by impermeable urban surfaces drives surface warming (Faisal et al., 2021). Our findings agree with other Bangladeshi studies: for example, areas with extensive built-up cover (like Gazipur and Dhaka) have shown significant LST increases, while vegetated areas remain cooler (Kulsum & Moniruzzaman, 2022; Rashid et al., 2022). The rising UTFVI values in these urban cores confirm increasingly severe thermal stress, matching similar trends found in Gazipur, where UTFVI rose from 0.39 to 0.49 over two decades (Salam et al., 2024). In short, expanding urbanization in Kushtia appears to have overwhelmed the district's natural cooling, driving a clear warming trend and higher urban heat exposure.

At the same time, population growth and urban densification have amplified heat sensitivity. The high- and medium-density classes expanded by nearly 50%, driven largely by Kushtia Sadar, which now contains most of the district's dense population. This concentration of people in the hottest areas increases the population's exposure to heat and their vulnerability. Such a pattern is well documented in Bangladesh: growing urban population density tends to coincide with loss of green space and rising LST (Adnan et al., 2024; Nawar et al., 2022). In practice, we see that wards of Kushtia municipality (which had >68% of the high-density expansion) overlap the zones of highest LST/UTFVI. This urban influx thus reinforces the heat risk, as seen in other cities (e.g., Dhaka, Chattogram, Narayanganj) where built-up growth drove both heat exposure and population vulnerability (Adnan et al., 2024; Mehrin et al., 2025; Rashid et al., 2022). In sum, increasing population density in Kushtia's towns has accentuated the sensitivity component of heat vulnerability, in line with analogous findings across rapidly urbanizing Bangladeshi cities.

Compounding the problem, the district's adaptive capacity (natural cooling from vegetation and water) has eroded markedly. The NDVI and NDWI values fell across Kushtia. The loss of green cover is especially evident – the area of even moderately healthy vegetation grew (0.2–0.5 NDVI class expansion) but mostly at the expense of the lowest-vegetation class, indicating replacement of sparse vegetation with either bare ground or urban land. However, it is important to note that the expansion of the Medium NDVI class does not necessarily represent an increase in dense or perennial natural vegetation. In Kushtia's predominantly agro-based landscape, February imagery coincides with active dry-season cropping, particularly irrigated Boro rice cultivation, which typically produces moderate NDVI values. Agricultural crops differ substantially from natural woody vegetation in canopy structure, rooting depth, evapotranspiration intensity, and seasonal permanence. Therefore, while moderate NDVI areas expanded, this likely reflects cropland intensification rather than a proportional enhancement of long-term ecosystem-based cooling capacity under the IPCC adaptive capacity framework.

Surface water has essentially vanished: the NDWI medium class disappeared entirely by 2024, which may be attributed to charland formation and river morphological changes that reduce stable surface water extent, along with the influence of dry-season image acquisition. These declines in “green and blue” infrastructure are consistent with findings by Hossain et al. (2025a) in Kushtia, who reported an 18% drop in NDVI and a 58% drop in NDWI district-wide from 1998 to 2023. Such degradation of vegetation and water bodies removes critical natural cooling. It is well established that vegetation mitigates heat via shading and evapotranspiration, so its loss drives temperatures higher (Soltanifard & Amani-Beni, 2025). Likewise, surface water (even incidental puddles or small wetlands) provides evaporative cooling – its disappearance further exacerbates heat. Thus, our observation that NDVI and NDWI have decreased is a logical cause of the rising LST and vulnerability. Global analyses agree that communities lacking tree canopy or water access suffer the highest heat risk (Dodman et al., 2023). In Kushtia, shrinking green-blue cover has clearly degraded the natural adaptive buffer against heat.

The multivariate relationships among indices reinforce these dynamics. We found a very strong inverse correlation between NDVI and LST ($r \approx -0.98$ overall), confirming that areas with more vegetation remain much cooler, a pattern seen elsewhere in Bangladesh (Rashid et al., 2022). Similarly, NDVI and population density are consistently negatively correlated ($r \approx -0.40$), reflecting that urban growth comes at the expense of green cover (Nawar et al., 2022). Interestingly, a very strong inverse relationship between NDVI and NDWI was observed in 2024 ($r = -0.99$). This reflects the strong biophysical coupling between vegetation greenness and surface moisture during the dry-season (February) conditions, when reduced water availability across agricultural fields, charland systems, and peripheral urban areas intensifies spectral contrast between vegetation and moisture signals. This pattern is further influenced by the heterogeneous land surface composition of the study area, which includes riverine charlands, irrigated croplands, and scattered water bodies, thereby amplifying the inverse NDVI–NDWI relationship. This finding is consistent with previous observations in the region (Hossain et al., 2025a). By contrast, built-up proxies (Albedo and UTFVI) show positive associations with population density and LST. For example, UTFVI hotspots align with major town centers, just as prior work found built-up districts exhibit higher heat exposure (Raja et al., 2021). Over time, the data show that vegetation and water conditions account for a growing share of environmental variability. Our PCA indicates that the first component (dominated by NDVI/NDWI) explained an increasing percentage of variance (51% in 2010, 63% in 2024), whereas the second component (dominated by LST/UTFVI) remained distinct. This suggests that spatial differences in greenery and moisture are

now the primary drivers of heat vulnerability patterns, while heat itself and population act as separate, secondary factors. In other words, the disruption of vegetation-water balance has become the dominant factor, which aligns with findings that loss of urban green is a principal determinant of UHI effects (Marando et al., 2022).

Finally, the combined heat vulnerability index reflects these trends: low-vulnerability areas have collapsed, and high-vulnerability areas have expanded dramatically. Between 2010 and 2024, the “Very High” and “High” vulnerability zones more than doubled (from 212 km² to 424 km²), while “Very Low/Low” areas fell by roughly 40%. This shift mirrors the compound impact of greater heat exposure and sensitivity alongside weakened adaptation. It is qualitatively similar to the evolution reported in other Bangladeshi cities: for instance, Dhaka’s HVI mapping found urbanized wards as heat hotspots and rising population as a key vulnerability factor (Adnan et al., 2024). In our case, by 2024, the most vulnerable zones are covered by much of the northern and central district, where urban density and heat coincide. A slight stabilization of the pattern (some southern areas showing moderate vulnerability) might indicate localized green rehabilitation or slower growth in those parts, but overall, the upward trend in heat vulnerability is unmistakable.

Overall, this study provides compelling evidence that Kushtia District is undergoing rapid thermal intensification driven by urban expansion, vegetation loss, and water depletion. The integrated geospatial and statistical analyses clearly show that the combined effects of rising LST, population densification, and declining NDVI–NDWI have collectively heightened heat vulnerability across the district. These findings are not isolated but consistent with broader national and global patterns of UHI amplification under unplanned development and ecological degradation (Adnan et al., 2024; Dodman et al., 2023; Rashid et al., 2022).

5. Conclusions

This study provides a comprehensive geospatial assessment of heat vulnerability dynamics across Kushtia District over a 14-year period (2010–2024), revealing a progressive intensification of thermal risk linked to rapid urban expansion and environmental degradation. The results demonstrate that LST increased by more than 5 °C, while NDVI and NDWI declined notably, indicating significant losses in vegetative and surface water cover. Correlation and PCA analyses jointly confirm that vegetation and surface moisture are the principal regulators of environmental variability and heat adaptation capacity, whereas urban and population factors exert secondary but enduring effects. The expansion of high and very high vulnerability zones further highlights the spatial spread of thermal stress within the district. These findings highlight the urgent need to integrate ecosystem-based urban planning and sustainable land management in Kushtia to mitigate the adverse impacts of rising surface temperatures. Implementing measures such as expanding urban green cover, conserving wetlands and waterbodies, and promoting reflective, climate-adaptive building materials can significantly reduce heat exposure and strengthen local resilience. Moreover, the study presents a replicable framework for assessing urban heat vulnerability in data-scarce regions, providing valuable insights to guide climate-resilient policy and adaptation planning for Kushtia and other rapidly urbanizing areas across Bangladesh. However, this study has certain limitations. Satellite imagery was acquired in February for seasonal consistency, which may underestimate peak pre-monsoon (May–June) heat intensity. Reliance on open-access Landsat data also limited image availability during peak summer due to cloud cover. The WorldPop dataset has an original resolution of 1 km and was resampled to 30 × 30 m only for raster alignment with satellite imagery; this does not increase its actual spatial precision and may introduce scale-related uncertainty. Furthermore, due to limited spatially explicit data, detailed socio-economic variables, such as income level, housing quality, and access to healthcare, could not be included. Therefore, the results primarily reflect environmental dimensions of spatial heat risk. Future research integrating higher-resolution demographic, socio-economic, and multi-seasonal datasets would improve assessment accuracy and provide a more comprehensive understanding of community-level heat risk.

Author Contributions

Conceptualization, M.R.I. and M.A.H.; methodology, M.R.I. and M.A.H.; validation, M.A.H.; formal analysis, M.R.I., T.Y., and R.S.; investigation, M.A.H.; data curation, M.R.I., T.Y., and R.S.; writing—original draft preparation, M.R.I., T.Y., R.S., and M.A.H.; writing—review and editing, M.A.H., M. H. M; visualization, M.R.I., T.Y., R.S., and M.A.H.; funding acquisition, M.H.M. All authors have read and agreed to the published version of the manuscript.

Data Availability

The data and images supporting our research results are included within the article or the Appendix.

Conflicts of Interest

The authors declare no conflicts of interest.

References

- Adnan, M. S. G., Kabir, I., Hossain, M. A., Chakma, S., Tasneem, S. N., Saha, C. R., Hassan, Q. K., & Dewan, A. (2024). Heatwave vulnerability of large metropolitans in Bangladesh: an evaluation. *Geomatica*, 76(2), 100020. <https://doi.org/10.1016/j.geomat.2024.100020>.
- Alam, S. (2024). *April temperatures in Bangladesh hottest on record*. Phys.org. <https://phys.org/news/2024-05-april-temperatures-bangladesh-hottest.html>
- Anand, V., Kaur, S., Rajput, V. D., Minkina, T., Mandzhieva, S., Kumar, S., Sharma, A., & Kumar, S. (2025). Analyzing the spatial relationship between land surface temperature and normalized difference vegetation index using remote sensing and GIS. *Discov. Geosci.*, 3(1). <https://doi.org/10.1007/s44288-025-00167-w>.
- Bangladesh Bureau of Statistics. (2023). *Population and Housing Census 2022: National Report (Volume 1)*. <https://bbs.gov.bd/pages/static-pages/6922e0ff933eb65569e297dc>
- Banglapedia. (2023). *Kushtia District*. http://en.banglapedia.org/index.php?title=Kushtia_District
- Begum, R. A., Lempert, R. J., Ali, E., Benjaminsen, T. A., Bernauer, T., Cramer, W., Cui, X., Mach, K., Nagy, G., Stenseth, N. C., et al. (2023). 1—Point of departure and key concepts. In *Climate Change 2022 – Impacts, Adaptation and Vulnerability* (pp. 121–196). Cambridge University Press. <https://doi.org/10.1017/9781009325844.003>.
- Cevik Degerli, B. & Cetin, M. (2023). Evaluation of UTFVI index effect on climate change in terms of urbanization. *Environ. Sci. Pollut. Res.*, 30(30), 75273–75280. <https://doi.org/10.1007/s11356-023-27613-x>.
- D’Ambrosio, V., Di Martino, F., & Miraglia, V. (2023). A GIS-based framework to assess heatwave vulnerability and impact scenarios in urban systems. *Sci. Rep.*, 13(1), 13073. <https://doi.org/10.1038/s41598-023-39820-0>.
- Dodman, D., Hayward, B., Pelling, M., Broto, V. C., Chow, W., Chu, E., Dawson, R., Khirfan, L., McPhearson, T., Prakash, A., et al. (2023). 6—Cities, settlements and key infrastructure. In *Climate Change 2022 – Impacts, Adaptation and Vulnerability* (pp. 907–1040). Cambridge University Press. <https://doi.org/10.1017/9781009325844.008>.
- Elgendy, D., Tolba, O., & Kamel, T. (2025). The impact of increasing urban surface albedo on outdoor air and surface temperatures during summer in newly developed areas. *Sci. Rep.*, 15, 26165. <https://doi.org/10.1038/s41598-025-08574-2>.
- Faisal, A.-A., Kafy, A.-A., Al Rakib, A., Akter, K. S., Jahir, D. M. A., Sikdar, M. S., Ashrafi, T. J., Mallik, S., & Rahman, M. M. (2021). Assessing and predicting land use/land cover, land surface temperature and urban thermal field variance index using Landsat imagery for Dhaka Metropolitan area. *Environ. Chall.*, 4, 100192. <https://doi.org/10.1016/j.envc.2021.100192>.
- Gessese, A. A. & Melesse, A. M. (2019). Temporal relationships between time series CHIRPS-rainfall estimation and eMODIS-NDVI satellite images in Amhara Region, Ethiopia. In *Extreme Hydrology and Climate Variability* (pp. 81–92). Elsevier. <https://doi.org/10.1016/b978-0-12-815998-9.00008-7>.
- Hossain, M. A., Haque, M. I., Parvin, M. A., & Islam, M. N. (2023). Evaluation of iron contamination in groundwater with its associated health risk and potentially suitable depth analysis in Kushtia Sadar Upazila of Bangladesh. *Groundw. Sustain. Dev.*, 21, 100946. <https://doi.org/10.1016/j.gsd.2023.100946>.
- Hossain, M. A., Islam, M. R., Yesmin, T., Sultana, R., Hossain, M. K., & Islam, R. (2025a). Spatiotemporal assessment of environmental change in Kushtia, Bangladesh (1998–2023) using remote sensing-based environmental indices. *Environ. Chall.*, 19, 101167. <https://doi.org/10.1016/j.envc.2025.101167>.
- Hossain, M. A., Rahman, M. M., Hasan, S. S., Mahmud, A., & Bai, L. (2025b). Analysis and forecasting of meteorological drought using PROPHET and SARIMA models deploying machine learning technique for southwestern region of Bangladesh. *Environ. Sustain. Indic.*, 27, 100761. <https://doi.org/10.1016/j.indic.2025.100761>.
- Huang, C., Liu, K., Ma, T., Xue, H., Wang, P., & Li, L. (2025). Analysis of the impact mechanisms and driving factors of urban spatial morphology on urban heat islands. *Sci. Rep.*, 15, 18589. <https://doi.org/10.1038/s41598-025-04025-0>.
- Kliengchuay, W., Phonphan, W., Niampradit, S., Kiangkoo, N., Srimanus, W., Niemanee, T., Arunplod, C., Wen, B., Guo, Y., Herbreteau, V., et al. (2025). Variation of vegetation cover and the relationship with land surface temperature across Thailand (2007 to 2022). *Sci. Rep.*, 15(1). <https://doi.org/10.1038/s41598-025-13018-y>.
- Kulum, U. & Moniruzzaman, M. (2022). Exploring the relationship of climate change and land-use dynamics with satellite-derived surface indices and temperature in greater Dhaka, Bangladesh. *J. Earth Syst. Sci.*, 131, 117. <https://doi.org/10.1007/s12040-022-01841-0>.
- Liang, S. (2001). Narrowband to broadband conversions of land surface albedo I: Algorithms. *Remote Sens. Environ.*, 76(2), 213–238. [https://doi.org/10.1016/S0034-4257\(00\)00205-4](https://doi.org/10.1016/S0034-4257(00)00205-4).
- Mahim, M. M. A., Rasel, M. I. A., Hasan, M. M., & Reza, A. H. M. S. (2025). Assessment of heatwave, drought, vegetation and moisture content using remote sensing and GIS: A comprehensive study in North-Western part of Bangladesh. *Nat. Hazards*, 121(12), 14563–14590. <https://doi.org/10.1007/s11069-025-07365-2>.

- Marando, F., Heris, M. P., Zulian, G., Udías, A., Mentaschi, L., Chrysoulakis, N., Parastatidis, D., & Maes, J. (2022). Urban heat island mitigation by green infrastructure in European Functional Urban Areas. *Sustain. Cities Soc.*, *77*, 103564. <https://doi.org/10.1016/j.scs.2021.103564>.
- Mehrin, M., Zuhra, F. T., & Rahman, M. M. (2025). Heatwave induced health vulnerability assessment in Bangladesh. *Environ. Res. Health*, *3*(1), 015007. <https://doi.org/10.1088/2752-5309/ada17d>.
- Nawar, N., Sorker, R., Chowdhury, F. J., & Rahman, M. M. (2022). Present status and historical changes of urban green space in Dhaka city, Bangladesh: A remote sensing driven approach. *Environ. Chall.*, *6*, 100425. <https://doi.org/10.1016/j.envc.2021.100425>.
- Patwary, M. M., Disha, A. S., Sikder, D., Hasan, S., Hossan, J., Bardhan, M., Billah, S. M., Hasan, M., Hasan, M., Haque, M. Z., et al. (2025). Urban heat stress and perceived health impacts in major cities of Bangladesh. *Int. J. Disaster Risk Reduct.*, *116*, 105066. <https://doi.org/10.1016/j.ijdr.2024.105066>.
- Raja, D. R., Hredoy, M. S. N., Islam, M. K., Islam, K. A., & Adnan, M. S. G. (2021). Spatial distribution of heatwave vulnerability in a coastal city of Bangladesh. *Environ. Chall.*, *4*, 100122. <https://doi.org/10.1016/j.envc.2021.100122>.
- Rashid, G. M., Akhter, M. A. E., & Mallik, M. A. K. (2024). The study of heat wave condition in Bangladesh during 1990 to 2019. *Atmosphere*, *10*, 88–97.
- Rashid, N., Alam, J. A. M. M., Chowdhury, M. A., & Islam, S. L. U. (2022). Impact of land use change and urbanization on urban heat island effect in Narayanganj city, Bangladesh: A remote sensing-based estimation. *Environ. Chall.*, *8*, 100571. <https://doi.org/10.1016/j.envc.2022.100571>.
- Rathi, S. K., Chakraborty, S., Mishra, S. K., Dutta, A., & Nanda, L. (2021). A heat vulnerability index: Spatial patterns of exposure, sensitivity and adaptive capacity for urbanites of four cities of India. *Int. J. Environ. Res. Public Health*, *19*(1), 283. <https://doi.org/10.3390/ijerph19010283>.
- Renard, F., Alonso, L., Fitts, Y., Hadjiosif, A., & Comby, J. (2019). Evaluation of the effect of urban redevelopment on surface urban heat islands. *Remote Sens.*, *11*(3), 299. <https://doi.org/10.3390/rs11030299>.
- Saha, P. & Gayen, S. K. (2025). A geospatial assessment of land use changes and their influence on land surface temperature in Koch Bihar district, West Bengal. *Results Earth Sci.*, *3*, 100089. <https://doi.org/10.1016/j.rines.2025.100089>.
- Salam, M., Islam, M. K., Jahan, I., & Chowdhury, M. A. (2024). Assessing the impacts of vegetation loss and land surface temperature on Surface Urban Heat Island (SUHI) in Gazipur District, Bangladesh. *Comput. Urban Sci.*, *4*(1). <https://doi.org/10.1007/s43762-024-00136-y>.
- Shahrujjaman, S. M., Sikder, B. B., Zahid, D., & Pal, B. (2025). Heat wave adaptation strategies among informal workers in an urban setting: A study in dhaka city, Bangladesh. *Nat. Hazards Res.*, *5*(3), 509–522. <https://doi.org/10.1016/j.nhres.2025.01.006>.
- Soltanifard, H. & Amani-Beni, M. (2025). The cooling effect of urban green spaces as nature-based solutions for mitigating urban heat: Insights from a decade-long systematic review. *Clim. Risk Manag.*, *49*, 100731. <https://doi.org/10.1016/j.crm.2025.100731>.
- Stevens, F. R., Gaughan, A. E., Linard, C., & Tatem, A. J. (2015). Disaggregating census data for population mapping using random forests with remotely-sensed and ancillary data. *PLoS One*, *10*(2), e0107042. <https://doi.org/10.1371/journal.pone.0107042>.
- Sun, Y., Li, Y., Ma, R., Gao, C., & Wu, Y. (2022). Mapping urban socio-economic vulnerability related to heat risk: A grid-based assessment framework by combing the geospatial big data. *Urban Clim.*, *43*, 101169. <https://doi.org/10.1016/j.uclim.2022.101169>.
- Tasumi, M., Allen, R. G., & Trezza, R. (2008). At-surface reflectance and albedo from satellite for operational calculation of land surface energy balance. *J. Hydrol. Eng.*, *13*(2), 51–63. [https://doi.org/10.1061/\(asce\)1084-0699\(2008\)13:2\(51\)](https://doi.org/10.1061/(asce)1084-0699(2008)13:2(51)).
- Uddin, M. N., Islam, A. S., Bala, S. K., Islam, G. T., Adhikary, S., Saha, D., Haque, S., Fahad, M. G. R., & Akter, R. (2019). Mapping of climate vulnerability of the coastal region of Bangladesh using principal component analysis. *Appl. Geogr.*, *102*, 47–57. <https://doi.org/10.1016/j.apgeog.2018.12.011>.
- World Bank Group. (2025). *Bangladesh Faces Health and Economic Risks from Rising Temperature: World Bank*. <https://www.worldbank.org/en/news/press-release/2025/09/16/bangladesh-faces-health-and-economic-risks-from-rising-temperature-world-bank>
- Yang, L., Cao, Y., Zhu, X., Zeng, S., Yang, G., He, J., & Yang, X. (2014). Land surface temperature retrieval for arid regions based on Landsat-8 TIRS data: A case study in Shihezi, Northwest China. *J. Arid Land*, *6*(6), 704–716. <https://doi.org/10.1007/s40333-014-0071-z>.
- Zhang, R., Jiang, A., & Jiang, L. (2025). Exposure-Sensitivity-Adaptability (ESA) framework based evaluation and characteristics analysis of urban disasters vulnerability in China. *Ecol. Indic.*, *176*, 113662. <https://doi.org/10.1016/j.ecolind.2025.113662>.
- Zhao, L., Fan, X., & Hong, T. (2025). Urban heat island effect: Remote sensing monitoring and assessment—Methods, applications, and future directions. *Atmosphere*, *16*(7), 791. <https://doi.org/10.3390/atmos16070791>.

Appendix

Table A1. Radiometric correction parameters and conversion equations for Landsat TM and OLI sensors

Processing Step	Landsat 4-7 (TM/ETM+)	Landsat 8-9 (OLI)
Data Format	8-bit DN (0-255)	16-bit DN (0-65535)
Radiance Conversion Equation	$L\lambda = \frac{(L_{max\lambda} - L_{min\lambda})}{(Q_{calmax} - Q_{calmin}) + L_{min\lambda}} \times (Q_{cal} - Q_{calmin})$	$L\lambda = ML * Q_{cal} + AL$
Radiance Parameters	L_{max} , L_{min} , Q_{min} , Q_{max} (provided in calibration metadata or literature)	ML (Radiance Multiplier) and AL (Additive term) from MTL file
Reflectance Equation	$\rho\lambda = \frac{(\pi * L\lambda * d^2)}{E_{sun\lambda} * \cos(\theta_s)}$	$\rho\lambda' = M_p * Q_{cal} + A_p$
Sun Angle Correction	$\cos(\theta_s)$	$\rho\lambda = \frac{\rho\lambda'}{\cos(\theta_s)}$
Reflectance Parameters	$E_{sun\lambda}$, Earth Sun distance (d), Solar zenith angle (θ_s)	M_p and A_p from MTL file

Table A2. Land Surface Temperature (LST) calculation steps and formula

Analysis	Formula	Definitions
Conversion DN to Radiance (Landsat-5 and Landsat-7)	$L\lambda = \frac{L_{MAX\lambda} - L_{MIN\lambda}}{(Q_{CALMAX} - Q_{CALMIN}) + L_{MIN\lambda}} * (Q_{CAL} - Q_{CALMIN}) + L_{MIN\lambda}$	<p>$L\lambda$ = Spectral radiance</p> <p>$L_{MAX\lambda}$ = Spectral radiance scaled to Q_{CALMAX} in (Watts/ (m² srμm))</p> <p>$L_{MIN\lambda}$ = Spectral radiance scaled to Q_{CALMIN} in (Watts/ (m² srμm))</p> <p>Q_{CAL} = Quantized calibrated pixel value in DN</p> <p>Q_{CALMAX} = Maximum quantized calibrated pixel value (corresponding to $L_{MAX\lambda}$) in DN</p> <p>Q_{CALMIN} = Minimum quantized calibrated pixel value (corresponding to $L_{MIN\lambda}$) in DN</p>
Top of atmospheric reflectance (TOA) (Landsat-8 and Landsat-9)	$L * Q_{cal} + AL$	<p>ML = Radiance multiplicative Band (No.10)</p> <p>AL = Radiance Add Band (No.10)</p> <p>Qcal = Quantized and calibrated standard product pixel values (DN)</p>
Convert Radiance into brightness temperature (BT)	$\frac{K2}{\left\{ \ln\left(\frac{K1}{L}\right) + 1 \right\}} - 273.15$	<p>K_1 = Band-specific thermal conversion was constant from the metadata.</p> <p>K_2 = Band-specific thermal conversion was constant from the metadata; L = TOA</p> <p>To obtain the results in Celsius, the radiant temperature is adjusted by adding the absolute zero (approx. - 273.15 °C)</p>
Proportion of vegetation (P_v)	$\left(\frac{NDVI - NDVI_{Min}}{NDVI_{Max} - NDVI_{Min}} \right)^2$	The minimum and maximum values of the NDVI image can be displayed directly in the image
Land surface emissivity (ϵ)	$0.004 * P_v + 0.986$	<p>P_v = Proportion of vegetation</p> <p>The value of 0.986 corresponds to a correction value of the Equation</p>
LST	$BT / 1 + W * (BT / 14380) * \ln(E)$	<p>BT = Top of atmosphere brightness temperature (°C)</p> <p>W = Wavelength of emitted radiance</p> <p>E = Land Surface Emissivity</p>

Table A3. Calculated PCA-weight for selected indices

Year	Indicator	PC1	Weight
2010	NDVI	-0.63	0.29
	LST	0.38	0.18
	UTFVI	0.35	0.16
	NDWI	0.49	0.23
	Albedo	0.30	0.14
	Population Density	-0.007	0.003

2017	NDVI	-0.58	0.27
	LST	0.30	0.14
	UTFVI	0.31	0.15
	NDWI	0.64	0.31
	Albedo	-0.24	0.12
2024	Population Density	0.014	0.007
	NDVI	0.68	0.35
	LST	-0.22	0.11
	UTFVI	-0.23	0.12
	NDWI	-0.62	0.32
	Albedo	0.20	0.10
	Population Density	-0.011	0.006

Table A4. District-wise areal coverage of vegetated land, waterbodies, surface albedo, population density, urban thermal field variance index, and ideal land surface temperature in Kushtia District across different years

Index	Year	Class name	Area Coverage (sq. km)
NDVI [Low (< 0.2) Medium (0.2 -0.5) High (≥ 0.5)]	2010	Low	810.22
		Medium	851.67
		High	2.19
	2017	Low	688.64
		Medium	975.37
		High	0.073
	2024	Low	560.97
		Medium	1100.42
		High	2.70
NDWI [Low (< 0.2) Medium (0.2 -0.5) High (≥ 0.5)]	2010	Low	1624.06
		Medium	40.02
		High	-
	2017	Low	1664.08
		Medium	-
		High	-
	2024	Low	1664.08
		Medium	-
		High	-
Albedo [Low (< 0.3) Medium (0.3- 0.6) High (≥ 0.6)]	2010	Low	1664.08
		Medium	-
		High	-
	2017	Low	1664.08
		Medium	0.0018
		High	-
	2024	Low	1662.91
		Medium	1.17
		High	-
Population density [Low (< 1,000) Medium (1,000–5,000) High (≥ 5,000)]	2010	Low	885.73
		Medium	723.47
		High	16.81
	2017	Low	752.62
		Medium	854.22
		High	19.17
	2024	Low	602.15
		Medium	999.10
		High	24.77
LST Low LST: < 25°C Medium LST: 25°C – 35°C High LST: > 35°C	2010	Low	1562.17
		Medium	101.9079
		High	-
	2017	Low	1434.498
		Medium	229.5792
		High	-
	2024	Low	793.6407
		Medium	870.4368
		High	-
UTFVI [Low (< 0.005) Medium (0.005–0.015) High (≥ 0.015)]	2010	Low	1143.86
		Medium	-
		High	520.2153
	2017	Low	1060.65
		Medium	98.49

	High	504.93
	Low	1039.65
2024	Medium	113.40
	High	511.0272

Table A5. Upazila-wise areal coverage of vegetated land, waterbodies, surface albedo, Population density, Urban Thermal Field Variance Index, and ideal land surface temperature in Kushtia District across different years

Index	Year	Class Name	Area Coverage (sq km)					
			Bheramara	Daulatpur	Khoksha	Kumarkhali	Kushtia	Mirpur
NDVI [Low (<0.2); Medium (0.2–0.5); High (≥0.5)]	2010	Low	68.59	172.59	41.07	180.513	223.57	123.88
		Medium	84.27	316.72	60.12	94.59	91.66	204.30
		High	0.19	1.31	0.054	0.234	0.06	0.34
	2017	Low	66.82	255.84	45.53	142.47	179.56	98.42
		Medium	86.23	334.75	55.72	132.85	135.73	230.076
		High	-	0.0243	-	0.0171	0.0045	0.027
	2024	Low	52.98	113.36	29.81	118.83	148.87	97.12
		Medium	100.08	376.42	71.43	156.50	166.43	229.56
		High	-	0.84	-	-	0.0009	1.85
NDWI [Low (<0.2); Medium (0.2–0.5); High (≥0.5)]	2010	Low	139.56	480.26	101.03	268.04	308.94	326.22
		Medium	13.50	10.35	0.22	7.30	6.36	2.31
		High	-	-	-	-	-	-
	2017	Low	153.06	490.62	101.25	275.34	315.30	328.53
		Medium	-	-	-	-	-	-
		High	-	-	-	-	-	-
	2024	Low	153.06	490.62	101.25	275.34	315.30	328.53
		Medium	-	-	-	-	-	-
		High	-	-	-	-	-	-
Albedo [Low (<0.3); Medium (0.3–0.6); High (≥0.6)]	2010	Low	153.06	490.62	101.25	275.34	315.30	328.53
		Medium	-	-	-	-	-	-
		High	-	-	-	-	-	-
	2017	Low	153.06	490.62	101.25	275.34	315.30	328.53
		Medium	-	0.0009	-	-	0.0009	-
		High	-	-	-	-	-	-
	2024	Low	153.03	489.73	101.25	275.15	315.29	328.47
		Medium	0.03	0.90	-	0.19	0.0009	0.06
		High	-	-	-	-	-	-
Population density [Low (<1,000); Medium (1,000– 5,000); High (≥5,000)]	2010	Low	44.91	274.93	22.23	144.77	173.75	202.22
		Medium	95.25	192.01	75.87	118.35	114.68	117.99
		High	1.23	-	-	1.39	13.99	0.06
	2017	Low	39.04	221.69	14.06	123.21	148.97	185.11
		Medium	100.83	245.24	84.03	139.53	137.88	135.03
		High	1.53	-	0.02	1.77	15.57	0.13
	2024	Low	30.20	163.78	4.54	95.27	134.59	154.94
		Medium	109.30	303.02	92.85	166.30	149.15	165.09
		High	2.0	0.13	0.72	2.93	18.69	0.23
UTFVI [Low (<0.005); Medium (0.005– 0.015); High (≥0.015)]	2010	Low	130.56	376.57	56.56	148.32	148.81	283.05
		Medium	-	-	-	-	-	-
		High	22.50	114.04	44.68	127.02	166.50	45.48
	2017	Low	123.07	358.55	41.80	118.70	132.76	285.77
		Medium	6.44	16.89	10.29	22.08	31.05	11.74
		High	23.55	115.17	49.15	134.56	151.48	31.02
	2024	Low	111.98	375.96	29.45	100.06	153.28	268.92
		Medium	7.68	17.52	12.70	26.15	33.15	16.21
		High	33.40	97.14	59.10	149.12	128.87	43.40
LST [Low (<25 °C); Medium (25 °C– 35 °C); High (>35 °C)]	2010	Low	149.02	435.11	99.36	256.90	297.12	324.64
		Medium	4.03	55.50	1.88	18.43	18.18	3.88
		High	-	-	-	-	-	-
	2017	Low	141.46	415.73	84.39	214.76	260.96	317.19
		Medium	11.59	74.89	16.86	60.57	54.34	11.33
		High	-	-	-	-	-	-
	2024	Low	88.78	323.39	12.20	58.29	88.16	222.80
		Medium	64.27	167.23	89.04	217.04	227.14	105.71
		High	-	-	-	-	-	-